energies

MDPI

Article

Numerical Study for Enhancement of Heat Transfer Using Discrete Metal Foam with Varying Thickness and Porosity in Solar Air Heater by LTNE Method

Rawal Diganjit [1], N. Gnanasekaran [1,*] and Moghtada Mobedi [2,*]

[1] Department of Mechanical Engineering, National Institute of Technology, Karnataka, Surathkal, Mangalore 575025, India
[2] Mechanical Engineering Department, Faculty of Engineering, Shizuoka University, 3-5-1 Johoku, Naka-ku, Hamamatsu-shi 432-8561, Japan
* Correspondence: gnanasekaran@nitk.edu.in (N.G.); moghtada.mobedi@shizuoka.ac.jp (M.M.)

Abstract: A two-dimensional rectangular domain is considered with a discrete arrangement at equal distances from copper metal foam in a solar air heater (SAH). The local thermal non-equilibrium model is used for the analysis of heat transfer in a single-pass rectangular channel of SAH for different mass flow rates ranging from 0.03 to 0.05 kg/s at 850 W/m^2 heat flux. Three different pores per inch (PPI) and porosities of copper metal foam with three different discrete thicknesses at equal distances are studied numerically. This paper evaluates the performance of SAH with 10 PPI 0.8769 porosity, 20 PPI 0.8567 porosity, and 30 PPI 0.92 porosity at 22 mm, 44 mm, and 88 mm thicknesses. The Nusselt number for 22 mm, 44 mm, and 88 mm thicknesses is 157.64%, 183.31%, and 218.60%, respectively, higher than the empty channel. The performance factor for 22 mm thick metal foam is 5.02% and 16.61% higher than for 44 mm and 88 mm thick metal foam, respectively. Hence, it is found that metal foam can be an excellent option for heat transfer enhancement in SAH, if it is designed properly.

Keywords: metal foam; local thermal nonequilibrium model (LTNE); forced convection; performance factor; solar air heater; single pass

Citation: Diganjit, R.; Gnanasekaran, N.; Mobedi, M. Numerical Study for Enhancement of Heat Transfer Using Discrete Metal Foam with Varying Thickness and Porosity in Solar Air Heater by LTNE Method. *Energies* **2022**, *15*, 8952. https://doi.org/10.3390/en15238952

Academic Editor: Gianpiero Colangelo

Received: 9 November 2022
Accepted: 22 November 2022
Published: 26 November 2022

1. Introduction

Solar energy is readily available in the environment, free of cost. Using fossil fuels for energy production affects our environment severely, and fossil fuels are non-renewable energy sources. We have to use clean energy sources to avoid these harmful effects. By using solar air collectors, solar energy can be converted into thermal energy. The solar air heater is simple in design and requires little maintenance [1–3]. Corrosion and leakage problems do not occur in solar air heaters. Because of their simplicity and low cost, they are widely used worldwide. The solar air heater involves low heat-capacity air and its efficiency is lower than that of the water heater [2,3]. Metal foam has a lower density, high structural strength, and high superficial area, and can increase convection due to which the heat transfer increases. Recently, the application of partially filled porous media, graded metal foam [4,5], or triangular porous media [6,7] have been required to increase the heat transfer in the system and to lower the cost. Nowadays, in solar applications, different porous media like metal foam [1,8–11], wire mesh [12–18], and spherical pebbles [15] are used to increase the temperature of the working fluid. Porosity and pore density are responsible for the enhancement of heat transfer, in addition to the thermal conductivity of the metal foam. These structural properties not only enhance heat transfer, but also increase the pressure drop [18]. In recent times, nano wires with carbon have enhanced the thermal conductivity due to large aspect ratio, and there has been an increase in the heat transfer rate [19]. The geometry of nanowires and their location affect absorption intensities in solar applications [20]. The silver nanowires are also a good option to increase the heat transfer in the solar power system. Ref. [21] Metal foam is one type of porous media used to enhance the temperature in the system. Metal foam has two types: open and closed cells. These types depend on whether the pores are sealed or not sealed. Open cell foam is a very homogenous structure that has almost constant properties. Copper and Aluminum metal foam are widely used in the system to enhance the heat transfer due to high thermal conductivity [8,22,23]. Dukhan and Quinones [24] observed that the effective conductivity and heat transfer of porous aluminum metal foam are more than a solid fin by 4% and 1.5%, respectively. They studied 10 PPI, 20 PPI, and 30 PPI with the porosity of 95% aluminum metal foam for heat transfer enhancement in SAH. Further, it has been observed that the number of pores per inch increases when heat transfer is more for the same porosity. Mancin et al. [25] studied the experimental heat transfer coefficient and pressure drop for five different copper metal foam samples. They noticed that heat transfer coefficient was more for higher mass flow rate and that pressure drop reduced with reduced porosity. The copper metal foam with 10 PPI and 0.905 porosity was found to be the best option for electronic cooling applications compared to 5, 20, and 40 PPIs and different porosities. Chen and Huang [26] reported a computational study of the heat transfer rate for solar water collector with the application of metal foam. They studied copper metal foam of different PPI with the same porosity at different heights of metal foam blocks. As the height of the metal foam increased, the Nusselt number also increased. Because of its higher thermal conductivity, copper has a higher heat transfer rate than aluminum or nickel. Kamath et al. [22] studied the heat transfer enhancement of aluminum and copper metal foams in the application of vertical channels. They conducted an experimental study for metal foam thicknesses of 10 mm, 20 mm and 30 mm and porosity ranging from 0.95 to 0.87. The 0.87 porosity of copper metal foam and 0.95 porosity of aluminum metal foam provides similar results for the same velocity and heat flux value. Bayrak and Oztop [23] studied the thermal performance of a solar air heater with aluminum metal at different thicknesses experimentally. They concluded that the 6 mm thickness aluminum metal foam has higher efficiency than 10 mm thickness metal foam for 0.025 kg/s mass flow rate. It is noted that aluminum metal foam gives better results than empty channel solar air heater for the same velocity and heat flux conditions.

Jouybari et al. [27] experimentally investigated the use of metal foam with the addition of nanofluid to improve thermal performance. The performance evaluation criteria are to reduce the pressure drop and increase the heat transfer. With the help of metal foam and nanofluid, the performance evaluation criteria increased more than 1% for lower flow rate. Further, the increase in nanofluid concentration increases the performance evaluation criteria. Saedodin et al. [28] reported experimental and numerical analysis of porous media in a Flat Plate Solar Collector (FPSC). The thermal efficiency increases by 18.5% with metal foam as porous media in a FPSC. Hussien and Farhan [29] investigated the thermohydraulic performance of SAH with three types of metal foam configurations. The corrugated metal foam gives higher thermal and effectiveness efficiencies, rather than longitudinal and staggered. A high heat transfer rate obtained for a higher PPI. Baig and Ali [30] proposed an experimental study on thermal storage in solar air heaters with the help of paraffin wax combined with aluminum metal foam. The analysis included four different configurations: flat plate, two copper ducts, four copper ducts, and the fourth configuration as a flat plate with pre-heat. Using two and four copper ducts gives more heat transfer than the other two configurations. A maximum efficiency of 97% was achieved with the help of a flat plate pre-heat configuration without a fan and with the help of aluminum foam and paraffin wax. Anirudh and Dhinakran [31] numerically studied metal foam blocks in the solar water heater (SWH). Different heights of metal foam blocks and 0.2 H, 0.6 H, and H of metal foam in the channel were considered where H is the channel height. It is observed that as the height of the metal foam increased, the performance of the SWH reduced, because pressure drop increases with height. Farhan et al. [32] performed a comparative study on the solid fin and metal foam. These types were further arranged in longitudinal, staggered, and corrugated configurations to check the heat transfer enhancement rate. It was noticed that the corrugated arrangement gives more heat transfer than does the other arrangements. Also, it was observed that the exergy loss and efficiency depend on the solar intensity and the velocity of air flowing through the channel.

Anirudh and Dhinakara [33] investigated the optimum performance of FPSC using different heights at inlet, test, and outlet sections of metal foam. The height at the inlet should be lower than the height at the outlet of the metal foam. Due to this arrangement, it gives less pressure drop, and improved efficiency. Kansara et al. [1] performed experiments in FPSC with internal fins and porous media. The authors showed that porous media has the highest heat transfer compared to fins and conventional SAH. Jadhav et al. [11] conducted numerical analysis of forced convection in the horizontal pipe in the presence of metal foam. They emphasized that the computational modelling of forced convection heat dissipation in the presence of high porosity and high thermal conductivity metallic foam. Rajarajeswari et al. [13] investigated numerical and experimental studies using single-pass flow. The diagonal arrangement of two wire mesh having different porosity was considered. The increase in thermal efficiency for 92.5% and 84.5% porosity is about 5–17% and 5–20%, respectively, with the mass flow rate ranging from 0.01 kg/s to 0.055 kg/s. A diagonal arrangement gives higher heat transfer compared to a parallel one. Jadhav [34] et al. studied the performance of the copper, aluminum, and nickel metal foams in a horizontal pipe. The performance factor increased with an increase in PPI. Table 1 gives the summary of previous arrangements of metal foams used in solar air heater.

The present study assumes that the test is conducted for open loop in clear sky days. The specified limit of the solar radiation, ambient temperature, air flow rate, air inlet temperature and temperature rise across solar air heater are ± 50 W/m^2, ± 1 °C, ± 1%, ± 0.1 °C, and ± 0.1 °C, respectively, for a 15 min duration. For example, RT-PT100 (manufactured by Heatron Indl. Heaters, Mangaluru, India) with tolerance of ± 0.1 °C and 16 Channel universal data logger (manufactured by Sunsui-DL-35, Pune, India) with accuracy of ± 0.08 °C are generally used to measure temperature at different points of the experimental apparatus in the study of Rajarajeswari et al. [9]. Hence the solar air heater is operated in steady state condition for the present study. Also, the average flux falling on the absorber plate for the month of April is 850 W/m^2. Here, 15 April is the mean of the value of solar intensity (IT) for the month of April. Similar assumptions are mentioned for test in [3]. The present study is selected for 0.3779, 0.3401, 0.3023, 0.2646, 0.2268, m/s, as mentioned in Rajarajeswari et al. [9]. The range of air velocity is less than 30% of the Mach number. Hence, the density variation is very much less, due to a velocity which is below 5%. So the flow is assumed to be a steady-state, incompressible turbulent flow. Similar assumptions are mentioned in [35].

The above literature shows that the metal foam arrangement in SAH improves the heat transfer rate, while at the same time the pressure drop increases when the inlet velocity increases. Instead of fully filled metal foams in the SAH, a discrete arrangement of metal foam reduces the pressure drop with reasonable heat transfer. There always exists a trade-off between the heat transfer and pressure drop as the inlet velocity of the fluid increases. Hence, to underline this situation, discrete metal foams with different thermal conductivity have been considered. Since the thickness of the metal foam in the discrete arrangement plays a significant role in heat transfer, the same has been varied while the distance between the discrete metal foams was kept constant. Moreover, the PPI of the metal foam is changed to see its effect in heat transfer and pressure drop. Hence in this paper, the following objectives are accomplished numerically: (i) to numerically design the SAH in ANSYS and use copper metal foam with discrete arrangement and different thicknesses, (ii) to compare different porosity of copper metal foam with different PPI and (iii) to analyze the best suitable metal foam amongst copper, aluminum, and nickel metal foams according to performance evaluation factor and pressure drop.

Table 1. Literature of metal foam as a porous media in solar air heater.

Ref.	LTE/LTNE	Methodology	Metal Foam Material	Pore Density	Pore Dia.	Porosity	Type of Arrangement of Metal Foam in SAH
[1]	LTNE	Expt. and Num-3D	Al	NM	2	0.92	Horizontal
[23]	NM	Expt.	Al	NM	NM	NM	Vertical–Staggered
[24]	NM	Theoretical–1D	Al	10 PPI, 20 PPI, 30 PPI	NM	0.95	Horizontal
[27]	LTE	Expt.	Cu	20	NM	0.93	Horizontal
[28]	LTE	Expt. and Num-2D	Cu	20	NM	0.93	Horizontal
[29]	NM	Expt.	Cu	15 PPI, 20 PPI	NM	NM	Fin configuration (i) longitudinal (ii) corrugated (iii) staggered
[30]	NM	Expt.	Al	NM	NM	NM	Horizontal
[32]	NM	Expt.	Cu	NM	NM	NM	(i) longitudinal, (ii) corrugated, (iii) staggered
[36]	LTE	Expt. and Num-2D	Al	NM	NM	0.90	Horizontal

Ref—Reference, LTE—local thermal equilibrium, LTNE—local thermal non equilibrium, NM—Not mentioned, Num—Numerical, Expt.—Experimental.

2. Theoretical (Analytical) Design of Solar Air Heater (SAH)

The theoretical design of the SAH was developed at the location of Mechanical Engineering Department, National Institute of Technology Surathkal Karnataka, India. For the conventional SAH, the material and properties are considered as mentioned in [13,37]. The dimensions mentioned in [13] are considered additional design parameters. As given in [2], based on Klein's recommendation, the mean value for the month in April is 15. Hence the analytical solution for the empty channel is done on 15 April at 13:00 PM, because, at this time, the solar radiation is maximum. The latitude and longitude of further study are 12°54′ N, 74°51′ E for the National Institute of Technology Karnataka, Surathkal. The analytical readings are considered during clear sky days in April 2022. Analytical studies are calculated under the climatic conditions of Surathkal, Karnataka, India (12.99° N, 74.81° E). The tilt angle of 13° with the ground surface facing south is taken for testing the SAH to achieve maximum solar radiation. The angle of tilt is equal to the latitude of that location, as mentioned in [13]. The constant a and b for monthly average daily global radiation are obtained for Mangalore city at 0.27 and 0.43, respectively, as mentioned in [2]. For the Surathkal location, wind speed, V_∞ is assumed as 1 m/s. The mean plate temperature is assumed as 323 K.

In this study, the absorber plate is considered as aluminum plate with 0.5 mm thickness. Aluminum is light in weight compared to copper, and its cost is also less than the copper plate. The insulation and frame are considered to be polyurethane foam and wood, respectively, for the present study. The toughened glass with 4 mm thickness is attached above the aluminum plate. The space between the glass and aluminum plate is 120 mm. The air flows through the space between glass and absorber plate. The detailed schematic diagram of the SAH is shown in Figure 1. Table 2 shows the material properties used during the simulation.

The present study is evaluated with similar velocities to [13]. The Reynolds number varies from 3287 to 5479. The material properties are considered to be isotropic. The detailed procedure followed for analytical calculation as explained in [2,3].

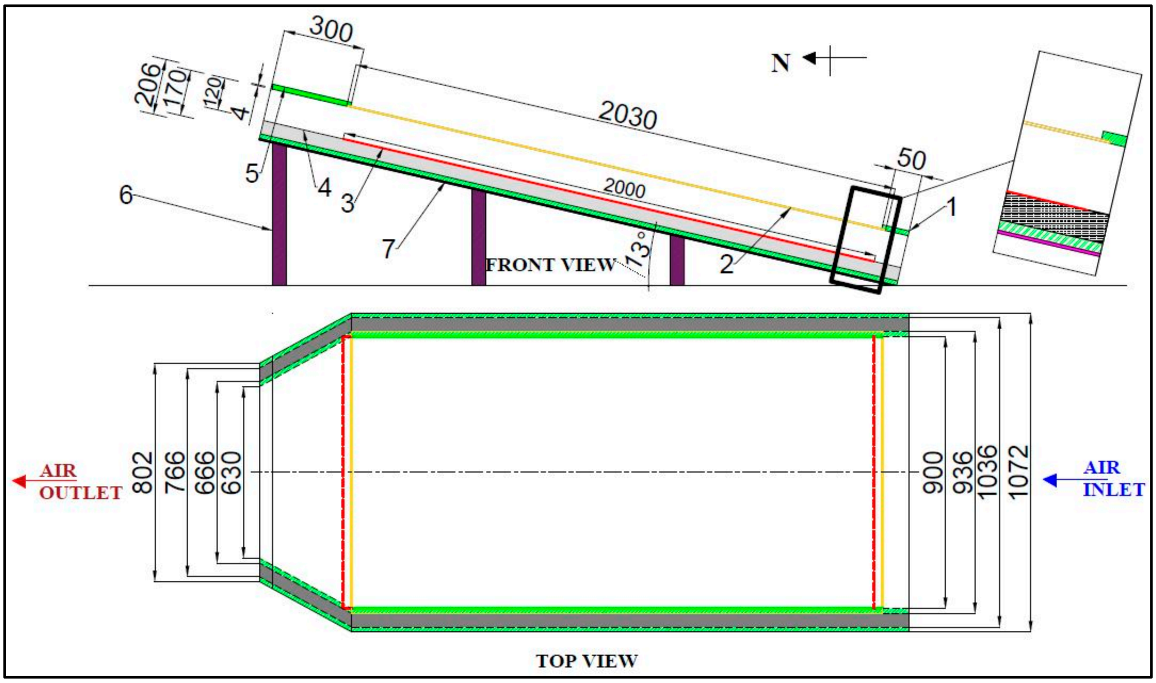

Figure 1. Detailed schematic layout of SAH: (1) wooden material for entrance section (in Green line), (2) toughened glass (in Yellow line), (3) aluminum absorber plate (Red line), (4) polyurethane foam (Grey hatch line), (5) wooden material for exit section (Green line), (6) M S steel stand for support (Purple line), and (7) wooden material (Green line) for the frame as an outer box of the solar air heater (All dimensions are in mm).

Table 2. Material properties considered for simulation [37,38].

Material	Density kg/m^3	Specific Heat (J/kg K)	Thermal Conductivity (W/m K)	Kinematic Viscosity (m^2/s)	Prandtl Number	Emissivity	Absorptivity
Air	1.225	1006.43	0.0242	1.79×10^{-5}	0.702	-	-
Alumium	2719	871	202.4	-	-	0.8	0.95
Glass	2500	670	0.7443	-	-	0.9	-
Wood	700	2310	0.173	-	-	-	-
Copper	8978	381	387.6	-	-	-	-
Nickel	8900	460.6	91.74	-	-	-	-

The following assumptions [13,37,39] are considered for analytical and numerical analysis of SAH:

1. The flow is considered steady state, two-dimensional and incompressible.
2. The thermo-physical properties of air are considered to be constant.
3. Inlet fluid temperature = 300 K.
4. Outlet pressure = P_{atm}.
5. I = 850 W/m^2.
6. Side walls are considered to be adiabatic. Negligible heat loss from the bottom plate and the periphery envelope to the surroundings. Negligible heat loss from the inlet and outlet surfaces.
7. The metal foam is an isotropic and homogeneous porous medium.

The analytical calculations of conventional solar air heater are done by the procedure mentioned in [2,3] as follows-

The monthly average daily inclined irradiance is calculated by following Equation (1) as

$$\delta \text{ (in degree)} = 23.45 \sin [0.9863(284 + n)] \quad (1)$$

where n is the day of the year, the present study for analytical is 15 April hence, n = 105. δ is the declination.

Equation (2) below calculates the value of the angle between an incident solar beam flux and the normal to a plane surface. Considering surface of solar air heater is facing south ($\gamma = 0^0$)

$$\mathrm{Cos}\,\theta = \sin\delta\sin(\phi - \beta) + \cos\delta\cos\omega\cos(\phi - \beta) \quad (2)$$

where θ is the angle between an incident solar beam flux and the normal to a plane surface. Φ is latitude of a location. β is the slope of the solar air heater with the horizontal surface.

The magnitude of ω_{st} for an inclined surface facing south is calculated by Equation (3)

$$|\omega_{st}| = \min[|\cos^{-1}(-\tan\varnothing\tan\delta)|,\ |\cos^{-1}\{-\tan(\varnothing - \beta)\tan\delta\}|] \quad (3)$$

The daily sunlight or sunshine hours per day is calculated from Equation (4) as

$$S_{max} = \frac{2}{15}\omega_{st} \quad (4)$$

The daily radiation fall on a horizontal surface at the location is calculated by Equation (5) as

$$H_0 = \frac{24}{\pi} I_{SC}(1 + 0.033\cos(\frac{360\,n}{365}))(\sin\omega_s\sin\phi\sin\delta + \cos\phi\cos\delta\sin\omega_s) \quad (5)$$

From Sukhatme et al. [2] constant a and b for Mangalore city in India are 0.27 and 0.43, respectively. Assuming the average sunshine hours per day are 9.5 h for April month. The monthly average of the daily global radiation a horizontal surface is calculated by Equation (6) as

$$\frac{\overline{H_g}}{H_o} = a + b(\frac{\overline{S}}{S_{max}}) \quad (6)$$

The monthly average daily diffuse radiation is calculated by Equation (7)

$$\frac{\overline{H_d}}{\overline{H_g}} = 0.8677 - 0.7365[\frac{\overline{H_g}}{\overline{H_o}}] \quad (7)$$

The hourly radiation on an inclined surface on nth day between 1 h is calculated by Equation (8) as

$$\begin{aligned} I_o = 1.367\left(1 + 0.033\cos\left(\tfrac{360\,n}{365}\right)\right)\sin\delta\sin(\phi - \beta) \\ + \cos\delta\cos\omega\cos(\phi - \beta)\,\tfrac{kW}{m^2} \end{aligned} \quad (8)$$

Normalizing factor f_c is mentioned in Equations (9) and (10)

$$\frac{\overline{I_g}}{\overline{H_g}} = \frac{\overline{I_o}}{\overline{H_o}}\frac{(a + b\cos\omega)}{f_c}\ \mathrm{kJ/m^2\text{-}h} \quad (9)$$

where

$$f_c = a + 0.5b[\frac{\frac{\pi\,\omega_s}{180} - \sin\omega_s\cos\omega_s}{\sin\omega_s - \frac{\pi\,\omega_s}{180}\cos\omega_s}] \quad (10)$$

The monthly average hourly diffuse radiation is calculated by Equation (11) as

$$\frac{\overline{I_d}}{\overline{H_d}} = \frac{\overline{I_o}}{\overline{H_o}} \quad (11)$$

The diffuse radiation is calculated by Equation (12) as

$$\frac{\overline{I_{dg}}}{\overline{H_d}} = \frac{\overline{I_o}}{\overline{H_o}} \tag{12}$$

Choose the maximum value of diffuse radiation (I_d) between Equations (11) and (12) for further calculations.

The beam radiation is calculated by Equation (13) as

$$I_b = I_g - I_d \tag{13}$$

The tilt factor for beam radiation (r_b) is calculated by Equation (14)

$$r_b = \frac{\cos\theta}{\cos\theta_z} = \frac{\sin\delta\ \sin(\varnothing-\beta) + \cos\delta\cos\omega\cos(\varnothing-\beta)}{\sin\varnothing\sin\delta + \cos\varnothing\cos\delta\cos\omega} \tag{14}$$

The tilt factor for diffuse radiation (r_d) is calculated by Equation (15)

$$r_d = \frac{(1+\cos\beta)}{2} \tag{15}$$

The tilt factor for reflector radiation (r_r) is calculated by Equation (16)

$$r_r = \frac{\rho(1-\cos\beta)}{2} \tag{16}$$

Assume ground reflectivity be 0.2. [2] The total flux (I_T) falling on tilted surface at any instant is calculated by Equation (17) as

$$I_T = I_b\, r_b + I_d r_d + (I_b + I_d)\, r_r\ (W/m^2) \tag{17}$$

The total flux (I_T) falling on tilted surface at any instant is calculated by flux coming on the surface of absorber plate i.e., flux incident on the transparent glass is passing through glass towards the black painted absorber plate. This flux is the addition of beam and diffuse radiation coming directly on the absorber plate and the radiation reflected onto the surface from surroundings. Here, all the solar radiation coming from the sun is absorbed by the absorber plate. The heated absorber plate transfers heat as heat flux to moving air from inlet to outlet with help of conduction, a convection mechanism neglecting radiation heat transfer. As mentioned in Sukhatme and Nayak [2], it is assumed that the heat flux i.e., solar intensity falling on the absorber plate is not more than $\pm$50 W/m^2 for a 15 min duration. Hence the solar air heater is working under a steady state condition.

The number of covers is considered for this solar air heater to be 1. The spacing between the plate is 120 mm. The top loss coefficient of solar air heater (U_t) is calculated by Equation (18)

$$U_t = \left[\frac{M}{\left(\frac{C}{T_{pm}}\right)\left(\frac{T_{pm}-T_a}{M+f}^{0.252}\right)} + \frac{1}{h_w}\right]^{-1} + \left[\frac{\sigma\,(T_{pm}^2 + T_a^2)(T_{pm}+T_a)}{\frac{1}{\varepsilon_p + 0.0425\ M\ (1-\varepsilon_p)} + \frac{2M+f-1}{\varepsilon_c} - M}\right] \tag{18}$$

where

$$f_t = \left(\frac{9}{h_w} - \frac{30}{h_w^2}\right)\left(\frac{T_a}{316.9}\right)(1 + 0.091M) \tag{19}$$

$$C_t = 204.429\ (\cos\beta)^{0.252}/d^{\ 0.24} \tag{20}$$

d is spacing (in m) between cover plate and absorber plate, h_w is the convective heat transfer coefficient at the top cover. The convective heat transfer coefficient at transparent cover is calculated by Equation (21)

$$h_W = 5.7 + 3.8V\infty \tag{21}$$

where σ is the Stefan Boltzmann constant, ε_p and ε_c is the emissivity of the absorber plate surface and bottom surface respectively.

The bottom loss coefficient of solar air heater (U_b) is calculated by Equation (22)

$$U_b = \frac{k_i}{\delta_b} \tag{22}$$

where k_i is the thermal conductivity of the insulation material and δ_b is the thickness of the insulation material.

The side loss coefficient is assumed as zero.

The overall loss coefficient (U_L) is calculated by Equation (23)

$$U_L = U_t + U_b + U_S \tag{23}$$

The transmissivity of the cover system of a solar air heater is calculated by Equation (24)

$$\tau = \tau_r\,\tau_a \tag{24}$$

where τ_r is the transmissivity obtained by considering only reflection and refraction, τ_a is the transmissivity obtained by considering only absorption.

The value of the convective heat transfer coefficient h_{fp} is calculated by using Equation (25)

$$h_{fp} = Nu\left(\frac{k_{air}}{\text{Hydraulic diameter }(d_h)}\right) \tag{25}$$

where Nu is Nusselt number, and k_{air} is the thermal conductivity of air

The Hydraulic diameter is calculated by Equation (26)

$$\text{Hydraulic diameter}(d_h) = \frac{4\,(W \times d)}{2\,(W + d)} \tag{26}$$

where, W is the width of the absorber plate and d is the spacing between the glass and absorber plate.

The average air velocity is calculated by Equation (27)

$$\text{Average air velocity} = \frac{\dot{m}}{\rho\,(W \times L)} \tag{27}$$

The Reynold number (Re) is calculated by Equation (28)

$$Re = \frac{\rho\,V\,d_h}{\mu} \tag{28}$$

The radiative heat transfer coefficient (h_r) is calculated as Equation (29)

$$h_r = \frac{\sigma}{\left(\frac{1}{\varepsilon_p} + \frac{1}{\varepsilon_b} - 1\right)}(T_{pm} + T_{bm})(T_{pm}^2 + T_{bm}^2) \tag{29}$$

where h_r is the radiative heat transfer coefficient, T_{pm} and T_{bm} is the mean temperature of the absorber plate and the bottom plate. It can be taken to be equal to the mean fluid temperature T_{fm}.

The effective heat transfer coefficient (h_e) between the absorber plate and the air stream is calculated by Equation (30)

$$h_e = h_{fp} + \frac{h_r\, h_{fb}}{h_r + h_{fb}} \tag{30}$$

The solar air heater efficiency factor is calculated Equation (31)

$$\acute{F} = (1 + \frac{U_L}{h_e})^{-1} \tag{31}$$

The useful heat gain rate for the solar air heater is calculated by Equation (32)

$$q_u = F_R\, A_P\, [S - U_l(T_{fi} - T_a)] \tag{32}$$

where F_R is the solar air heater heat removal factor, S is the flux absorbed in the absorber plate.

$$F_R = \frac{\dot{m}\ C_p}{U_L\ A_P}\,[1 - \exp\{-\frac{F'\, U_l\, A_P}{\dot{m}\, C_P}\}] \tag{33}$$

$$S = I_T(\tau\alpha)_{avg} \tag{34}$$

The instantaneous efficiency of the solar air heater is calculated by Equation (35)

$$n_i = \frac{q_u}{I_T A_C} \tag{35}$$

The outlet temperature of the solar air heater is obtained by Equation (36)

$$q_u = \dot{m} C_P (T_{fo} - T_{fi}) \tag{36}$$

The pressure drop across the collector is calculated by Equation (37)

$$\text{Pressure drop } (\Delta P) = \frac{4\, f\, \rho L V^2}{2\, d_h} \tag{37}$$

where f is the friction factor, L is the length of SAH.

The detailed information of analytical calculation is mentioned in [2,3]. All the calculations are done with the help of Microsoft Excel.

3. Numerical Modelling and Meshing

All the design and analysis are performed in ANSYS Fluent 2022 R2 software. The empty channel and porous bed analysis are done for the same heat flux, i.e., the same solar intensity falling on the SAH. The dimensions and material properties of SAH, governing equations, methodology, and assumptions are considered as mentioned in [9,10,37,40]. Figure 2 shows the metal foam arrangement adopted for numerical study. Figure 3 is meshing done for 88 mm metal foam thicknesses. The detailed boundary conditions used during simulation are mentioned in Table 3. k-ε viscous model is used in ANSYS Fluent for this study. The planar-space steady-state pressure-based solver with double precision is considered for 2D analysis. A Green Gauss node-based method is used for the gradient to discretize the convection and diffusion terms. A second-order upwind scheme is applied to discretize pressure, momentum, Turbulent kinetic energy, turbulent dissipation

The under-relaxation factors for pressure, momentum, turbulent kinetic energy, turbulent dissipation rate, turbulent viscosity, and energy are taken as 0.3, 0.7, 0.8, and 1, respectively. The relaxation factors for other terms are kept in unity by default. In solution initialization, standard initialization method is selected with computing from the inlet. The convergence criteria set for energy is 10^{-6}, while for other terms it is set as 10^{-5}.

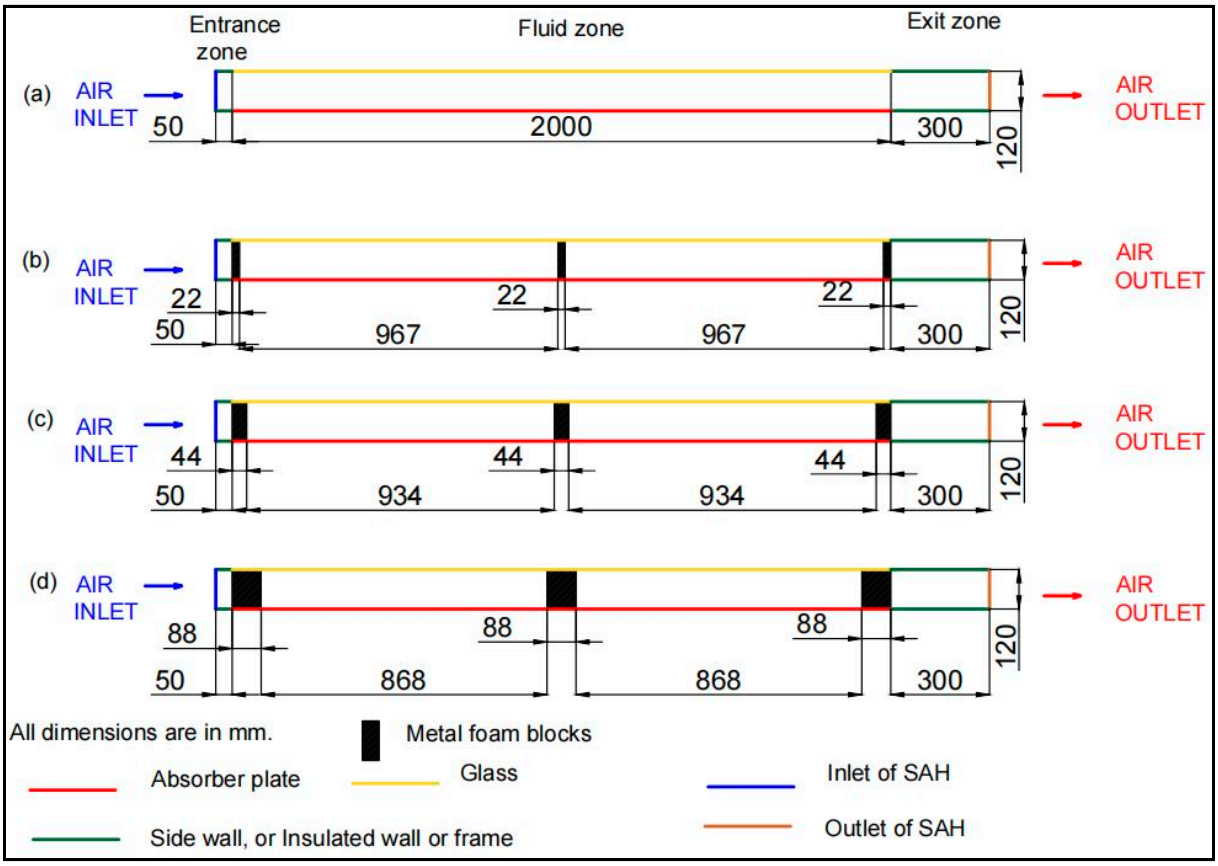

Figure 2. Schematic of SAH: (**a**) empty channel SAH, (**b**) 22 mm filled metal foam SAH, (**c**) 44 mm filled metal foam SAH (**d**) 88 mm filled metal foam SAH.

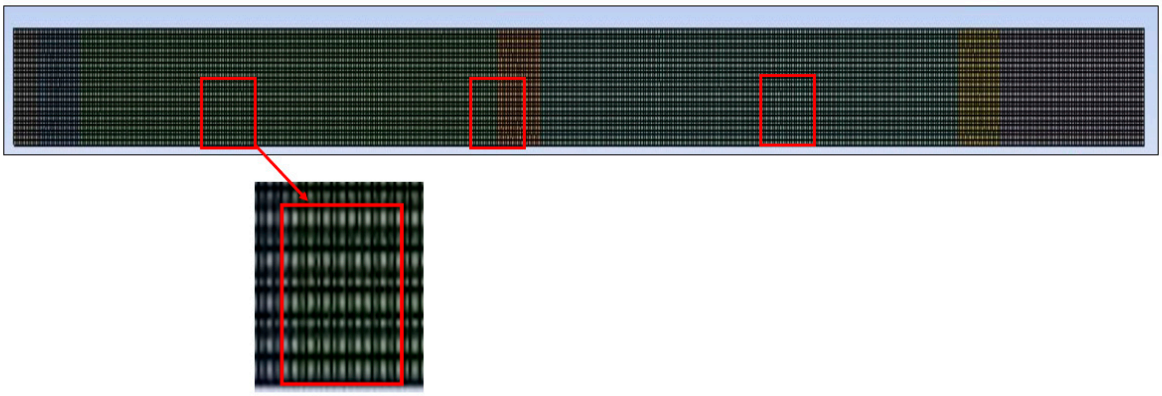

Figure 3. Quadrilateral mesh of 88 mm metal, foam block, solar air heater.

Grid Sensitivity Analysis

The minimum size of the mesh is achieved by grid sensitivity analysis. Table 4 shows the details of the number of elements and its skewness. The simulations are performed for four different mesh sizes. The temperature variation and change in pressure are shown in Table 4. The maximum number of elements is set as baseline and other elements are compared with it. From the results, 125,280 elements are preferred for further computational investigation because it has less deviation than other mesh sizes.

Table 3. Boundary conditions used during simulation in SAH [2,13,14,17,37].

	Momentum	**Thermal**	
Absorber plate	Stationary wall No slip shear condition	Heat flux = 850 W/m^2 Material = Aluminium Wall Thickness = 0.0005 m Bottom of the wall	
Glass	Stationary wall No slip shear condition	Mixed Heat transfer coefficient (HTC) = 9.5 W/m^2 as wind speed assumed as 1 m/s Free stream temperature = 300 K External emissivity = 0.88 External radiation temperature = 300 K Wall thickness = 0.004 m	Equation considered as h_w = 5.7 + (3.8 V_∞)
Side wall and other wall	Stationary wall No slip shear condition	Heat flux = zero W/m^2 i.e., adiabatic wallMaterial = wood Wall thickness = 0.018 m	
Inlet	Velocity magnitude as 0.3779, 0.3401, 0.3023, 0.2646, 0.2268, m/s	Inlet temperature = 300 K	
Outlet	Pressure outlet as zero	Back flow temperature = 300 K	

Table 4. Mesh generation.

Number of ELEMENTS	**Max Skewness**	**Outlet Temperature, T_{out}, K**	**Pressure Drop ΔP, Pa**	**T_{out} Deviation (%)**	**ΔP Deviation (%)**
70,499	0.273	334.41	0.053	0.2	0
92,652	0.278	334.45	0.053	0.009	0
125,280	0.004	334.47	0.053	0.002	0
180,480	0.0036	334.48	0.053	Baseline	

4. Governing Equations and Turbulence Modelling

For fluid flow in solar air heater, continuity and Reynolds-Averaged-Navier-Stocks (RANS) equations are used. In this study, the Renormalization group (RNG) k-ε turbulence model with enhanced wall treatment [13,14,17,38] is used, as it improves the performance for rotation and streamline curvature.

Continuity equation for empty channel is mentioned in Equation (38a)

$$\frac{\partial(\rho u_j)}{\partial x_i} = 0 \tag{38a}$$

Continuity equation for metal foam is mentioned in Equation (38b)

$$\frac{\partial(\rho \varepsilon u_j)}{\partial x_i} = 0 \tag{38b}$$

Momentum equation for empty channel is mentioned in Equation (39a)

$$\frac{\partial}{\partial x_j}(\rho u_i u_j) + \frac{\partial p}{\partial x_i} = \frac{\partial}{\partial x_j}\left[\mu\left(\frac{\partial u_i}{\partial x_j} + \frac{\partial u_j}{\partial x_i}\right)\right] \tag{39a}$$

Momentum equation for metal foam channel is mentioned in Equation (39b)

$$\frac{\partial}{\partial x_j}(\rho u_i u_j) + \varepsilon\frac{\partial p}{\partial x_j} = \frac{\partial}{\partial x_j}\left[\mu\left(\frac{\partial u_i}{\partial x_i} + \frac{\partial u_j}{\partial x_j}\right) - \varepsilon\left(\frac{\mu_{eff}}{K}\mu_i + \rho C|u|u_i\right)\right] \tag{39b}$$

Here, K is the permeability and C is the inertia coefficient.

Energy equation for fluid in empty channel,

$$\frac{\partial}{\partial x_i}(\rho u_j T) - \frac{\partial}{\partial x_j}\left[\lambda_f \frac{\partial T}{\partial x_J}\right] = 0 \tag{40}$$

To model flow through porous media in non-equilibrium thermal model, for simulations solid porous zone and fluid zone are not in thermal equilibrium. Hence, these two zones are interacted with heat transfer only.

For fluid zone equation as:

$$\varepsilon\frac{\partial\left(\rho C_P u_j T\right)}{\partial x_j} = \lambda_{fe}\varepsilon\frac{\partial}{\partial x_j}\left(\frac{\partial T_f}{\partial x_j}\right) + h_{sf}a_{sf}(T_S - T_f) \tag{41}$$

For solid zone equation as:

$$\lambda_{se}(1-\varepsilon)\frac{\partial}{\partial x_j}\left(\frac{\partial T_s}{\partial x_j}\right) = h_{sf}a_{sf}(T_s - T_f) \tag{42}$$

where,

$$\lambda_{fe} = \lambda_f \cdot \varepsilon \text{ and } \lambda_{se} = \lambda_s \cdot (1-\varepsilon)$$

In this study, to obtain the characteristics of porous media for solar air heater, a Darcy Extended Forchheimer (DEF) flow model is considered. The source term is added with the help of a viscous loss term and aninertial loss term. The DEF model is further joined with momentum equation as a source term. The inertial and viscous loss terms are calculated with the help of permeability and form drag coefficient of porous media. Calmidi and Mahajan [40] have proposed metal foam properties as superficial area density and interfacial heat transfer coefficient, which are given by Equations (43) and (44).

Superficial area density

$$a_{sf} = \frac{3\pi d_f\left(1 - \exp^{-\left(\frac{1-\varepsilon}{0.04}\right)}\right)}{(0.59 d_P)^2} \tag{43}$$

Interfacial heat transfer coefficient

$$\frac{h_{sf}d_f\left(1 - \exp^{-\left(\frac{1-\varepsilon}{0.04}\right)}\right)}{\lambda_f} = \begin{cases} 0.76 Re_{d_f}^{0.4} Pr^{0.37}, (1 \le Re_{d_f} \le 40) \\ 0.52 Re_{d_f}^{0.5} Pr^{0.37},\ (40 \le Re_{d_f} \le 10^3) \\ 0.26 Re_{d_f}^{0.6} Pr^{0.37},\ (10^3 \le Re_{d_f} \le 2\times 10^5) \end{cases} \tag{44}$$

where λ_f is the thermal conductivity of working fluid, Pr is the Prandtl number, Re_{df} is known as Reynolds number calculated by the fiber diameter of the metal foam. It is calculated from following Equation (45).

$$Re_{d_f} = \left\{ u d_f\left(\frac{1 - \exp^{-\left(\frac{1-\varepsilon}{0.04}\right)}}{\varepsilon\upsilon}\right) \right\} \tag{45}$$

where d_f is the fiber diameter in m, and d_P is the pore diameter in m.

The properties of metal foam, for example fiber diameter, permeability, pore size and inertial coefficient are determined by Table 5. The detailed information on porous media metal foam is described in [11,22,34]. Table 6 gives the copper metal foam properties considered for present study. The volume of the present porous metal foam block is considered a continuum with homogenous properties with respect to porosity and pore size. The similar homogeneous properties are considered in previous literature. The solid metal foam assumed here is gray and optically thick considering its absorption, isotropic scattering and emission properties throughout the length is same. The representative elementary volume (REV) analysis is important to get more information about heat and/or fluid flow in the porous medium or to determine volume average transport parameters (such as permeability, inertia coefficient, interfacial heat transfer coefficient etc.) or do a pore-scale study including voids and struts in the computational domain requiring extremely long computational time. To reduce the computational time and complexities in smaller size of pores in present porous media, it has uniform mixed medium of air as fluid and metal foam. As per REV scale simulation, it is not necessary to detailed accurate dimensions of porous block. Hence, the flow of air in metal foam is laminar and incompressible. The volume difference between metal foam before heating and after heating due to solar intensities are ignored [41,42].

Table 5. Properties and its correlations of metal foam [11,40].

Sr. No	Properties	Correlations
1	Pore size (d_p)	$d_p = \frac{0.0254}{PPI}$
2	Fiber diameter (d_f)	$\frac{d_f}{d_p} = 1.18\sqrt{\frac{(1-\varepsilon)}{3\pi}}\left(\frac{1}{1-e^{\left(\frac{(1-\varepsilon)}{0.04}\right)}}\right)$
3	Permeability (K)	$K = 0.00073(1-\varepsilon)^{-0.224}\left(\frac{d_f}{d_p}\right)^{-1.11} d_p^2$
4	Inertial/form coefficient (CI)	$CI = 0.00212(1-\varepsilon)^{-0.132}\left(\frac{d_f}{d_p}\right)^{-1.63}$

Table 6. Properties of metal foam [11,40].

PPI	Fiber Diameter	Pore Diameter	Porosity	Viscous Resistance	Inertial Resistance	Interfacial Area Density	Heat Transfer Coefficient
10	0.687	4.644	0.8769	1.742×10^{-7}	176.75	824.2496	85.8858
20	0.619	3.837	0.8567	2.490×10^{-7}	217.04	1106.8362	91.2402
30	0.703	4.732	0.92	1.644×10^{-7}	148.97	936.38	178.908

For all the cases, the inlet temperature is kept constant as the ambient temperature. The outlet is modelled as a pressure outlet with gauge pressure as zero Pascal. The turbulent intensity is specified as Equation (46)

$$I = 0.16\ (Re)^{-1/8}\ \text{in percentage} \tag{46}$$

The bulk mean fluid temperature is calculated as mentioned in Equation (47)

$$T_{\text{bulk mean}} = \frac{T_i + T_o}{2} \tag{47}$$

where T_i is the inlet temperature of the air in K, T_o is the outlet temperature of the air in K.

The convective heat transfer coefficient (h) in W/m^2 K is calculated by Equation (48) as

$$h = \frac{q_W}{T_{abs} - T_{\text{bulk mean}}} \tag{48}$$

where q_W is the useful heat gain for solar air heater in W/m^2, T_{abs} is the absorber plate temperature in K,

The average heat transfer coefficient ($\overline{h}$) is calculated by Equation (49),

$$\overline{h} = \frac{\sum_1^N h}{N} \tag{49}$$

where the N is the total number of samples or heat transfer coefficient obtained at the particular velocity.

The Nusselt number is calculated by the Equation (50) as

$$Nu = \frac{hD_h}{k_{air}} \quad (50)$$

where Nu is the Nusselt number, h is the heat transfer coefficient in W/(m^2 K), D_h is the hydraulic diameter in m, and k_{air} is the thermal conductivity of air in W/(m K).

The average Nusselt number is calculated by the Equation (51) as

$$\overline{Nu} = \frac{\overline{h}D_h}{k_{air}} \quad (51)$$

where $\overline{Nu}$ is the average Nusselt number, and $\overline{h}$ is the average heat transfer coefficient in W/(m^2K).

D_h is the hydraulic diameter in m, k_{air} is the thermal conductivity of air.

The friction factor (f) across the SAH is calculated by Equation (52) with the help of pressure drop across the rectangular channel i.e., inlet pressure and outlet pressure.

$$f = \frac{2\rho_f \Delta P D_h}{u^2 L} \quad (52)$$

where the ρ_f is the density of fluid in kg/m^3, ΔP is the difference of pressure between inlet pressure and outlet pressure in Pa, D_h is the hydraulic diameter in m, u is velocity of air in m/s, and L is the length of the SAH in m.

The heat transfer enhancement ratio for a solar air heater is calculated based on Equation (53)

$$\text{Heat transfer enhancement ratio} = \frac{Nu_P}{Nu_E} \quad (53)$$

where Nu_P is the Nusselt number of porous media and Nu_E is the Nusselt number of empty channels.

The performance factor is calculated by Equation (54) as

$$\eta_p = \frac{j}{f^{1/3}} \quad (54)$$

where η_P is the performance factor, j is the Colburn j factor, and f is the friction factor.

5. Results and Discussion

5.1. Verification and Validation of Empty Channel Solar Air Heater

For accurate analysis, the flow of working fluid in the empty channel within the glass and the absorber plate of the test section is essential. The solar radiation first falls on the glass then is transmitted through the glass. Further, this solar intensity is absorbed by the black-painted absorber plate. The air is flowing through the space available between the glass plate and absorber plate, which is 120 mm in the present study. Consequently, air gets heated from the glass as well as the absorber plate. The effect of it shows that the outlet temperature increases. For the Nusselt number relations, when air as a fluid is passing through the two parallel smooth plates, i.e., glass and absorber plate for lower Reynolds number (3000 to 7500) are calculated by relation of the Gnielinski equation as mentioned in [43]. Hence, the correlation of Gnielinski in terms of Nusselt number (Nu) and the correlation of Blasius and Petukhov in terms of friction factor (f) is applied to validate the flow characteristic of turbulent flow in the test section. The validated results of heat transfer and friction factor are shown in Figure 4a,b, respectively. A comparison between Nu and f obtained from the CFD results with the correlation given in Table 7. In Figure 4a,b, the CFD results are in good agreement with the correlations, and the results also showed that the Nu number is directly proportional to the Reynolds number and the friction factor is inversely proportional to the Reynolds number. The correlation and numerical results have similar trends for Nusselt number and friction factor in Figure 4a,b, respectively.

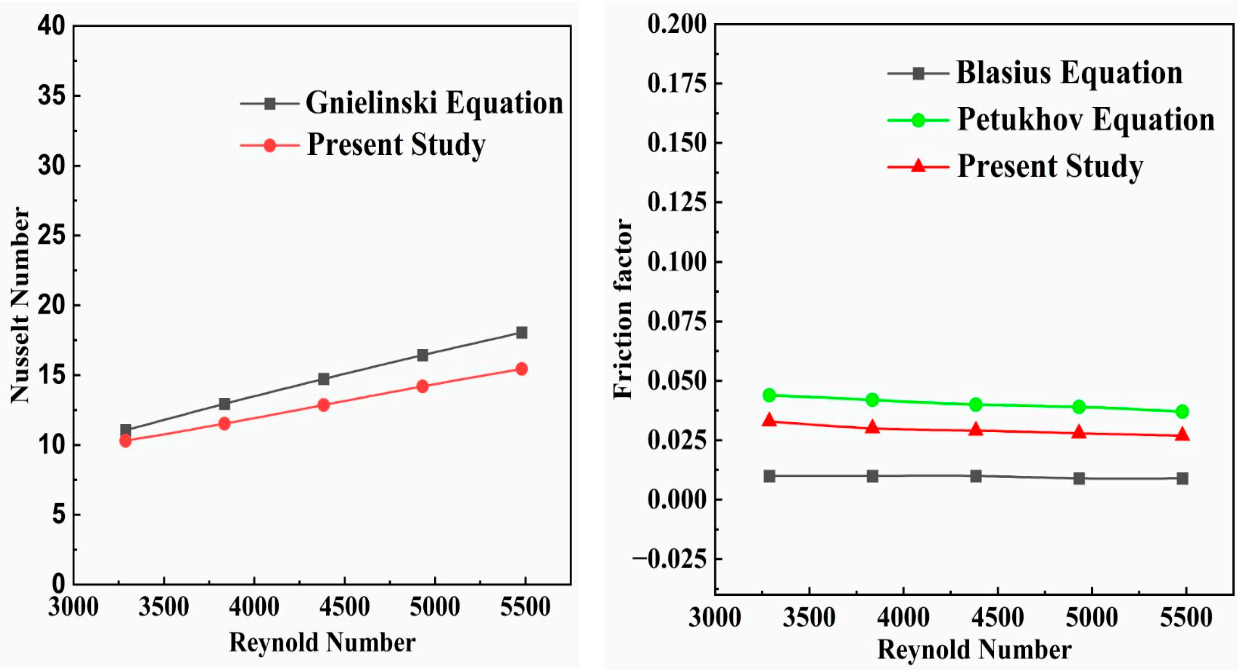

(**a**) (**b**)

Figure 4. (**a**)Verification of Nusselt number for empty channel of solar air heater. (**b**) Verification of friction factor for empty channel of solar air heater.

Table 7. Correlation equations for the verification of the empty channel SAH.

Name	Correlation Equation	Reference
Gnielinski	$Nu = \frac{(f/8)(Re-1000)\ Pr}{1+12.7(f/8)^{0.5}\ (Pr^{2/3}-1)}$ for $3000 < Re < 7500$	
Petukhov	$f = (0.790 \ln Re - 1.64)^{-2}$ for $3000 < Re < 5\times10^{6}$	[2,3,14,17,37,43]
Blasius	$f = 0.079Re^{0.25}$	

5.2. Validation Part

The analytical and numerical results of the present study are similar to the conventional SAH [13]. The average deviation between the analytical and CFD results with K Rajarajeswari et al. [13] is 9.66%. Figure 5 shows that as the mass flow rate increases, the temperature difference between outlet and inlet gives less deviation. The analytical and numerical studies show a similar trend. The average deviation between the analytical and CFD results is 2.78%. The detailed procedure followed for analytical calculation is as explained by Equations (1) to (37) and mentioned in [2,3].

5.3. Effect of Velocity Distribution along the Length of the Channel

The velocity distribution for 0.3779, 0.3401, and 0.3023 m/s of 30 PPI 0.92 porosity is presented in Figure 6. The figure shows that the velocity in the middle of the channel is maximum. The line path for all the velocities shows a parabolic curve for 88 mm thick copper metal foam.

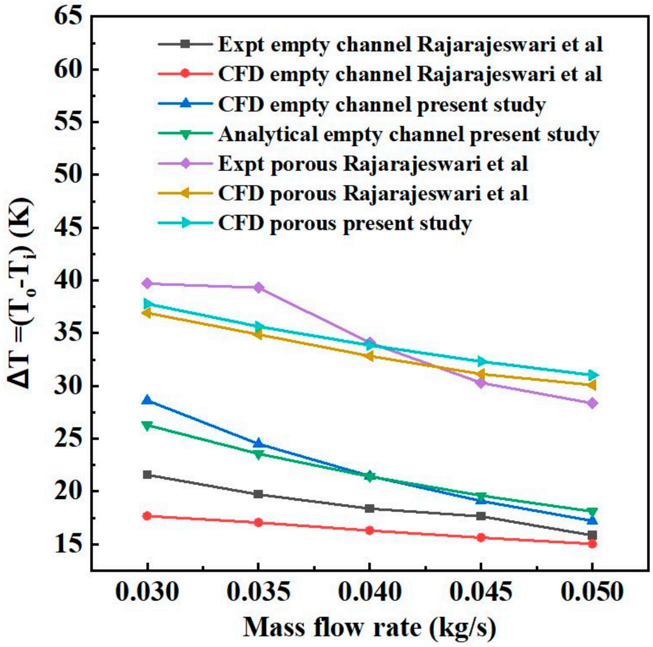

Figure 5. Validation of analytical and CFD results of present empty channel SAH with Rajarajeswari et al. [13].

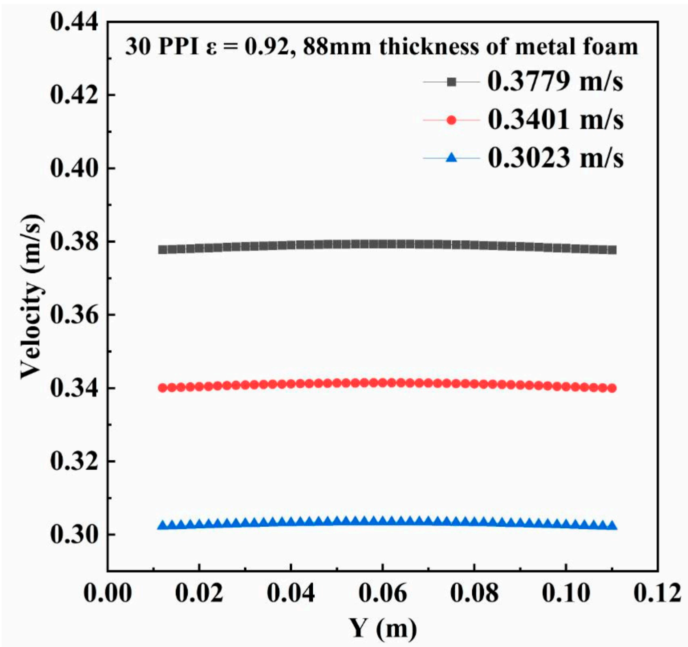

Figure 6. Velocity profile for 30 PPI 0.92 porosity with 88 mm thickness metal foam at three different velocities.

5.4. Temperature Distribution and Velocity Distribution for Different Thickness

Figure 7a–c presents the temperature contour relative to 0.92 porosity 30 PPI Copper metal foam for 0.3779 m/s velocity for the thicknesses of 22 mm, 44 mm, and 88 mm. In the case of porous media such as metal foam, the maximum temperature represents the temperature near the absorber plate. In the case of the lower thickness of the metal foam, the absorber plate temperature is higher, as shown in Figure 7. The temperature is uniform throughout the channel except near the absorber plate. For the same PPI and porosity, as the thickness of the metal foam increases, the absorber plate temperature decreases due to more heat transfer area.

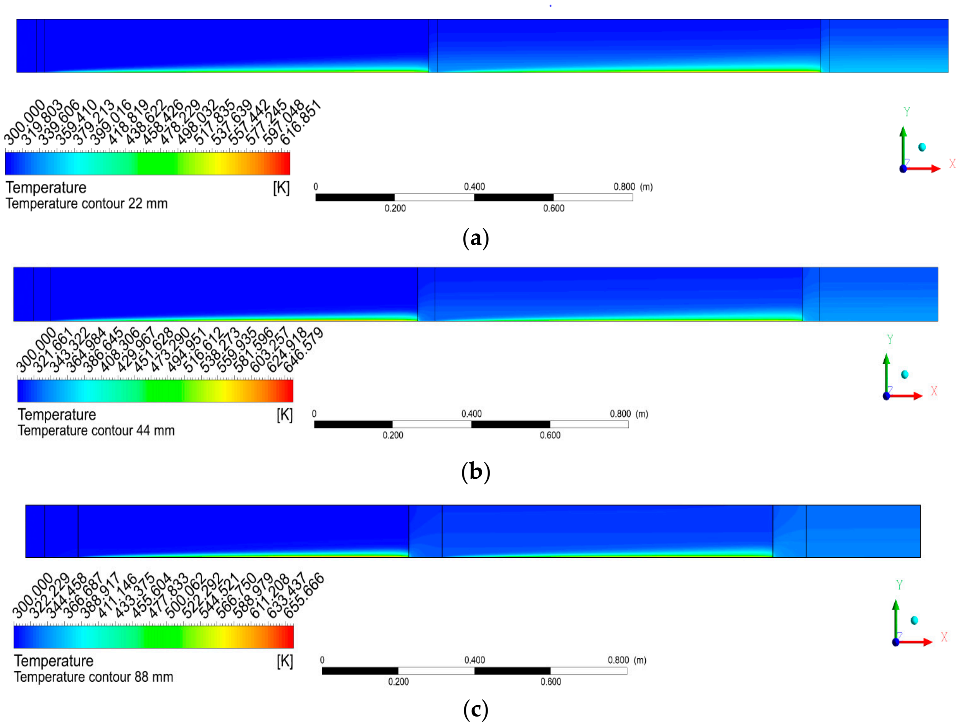

Figure 7. Contour of temperature for 30 PPI 0.92 porosity copper metal foam at 0.3779 velocity of (**a**) 22 mm, (**b**) 44 mm and (**c**) 88 mm thick metal foam.

5.5. Velocity Distribution for Different Thickness

Figure 8 represents the velocity distribution for 0.3779 m/s velocity for 30 PPI 0.92 porosity copper metal foam at (a) 22 mm, (b) 44 mm and (c) 88 mm thick metal foam. Figure 8a–c shows the maximum velocity in the middle of the channel. The velocity near the wall is close to zero because of the shear resistance effect.

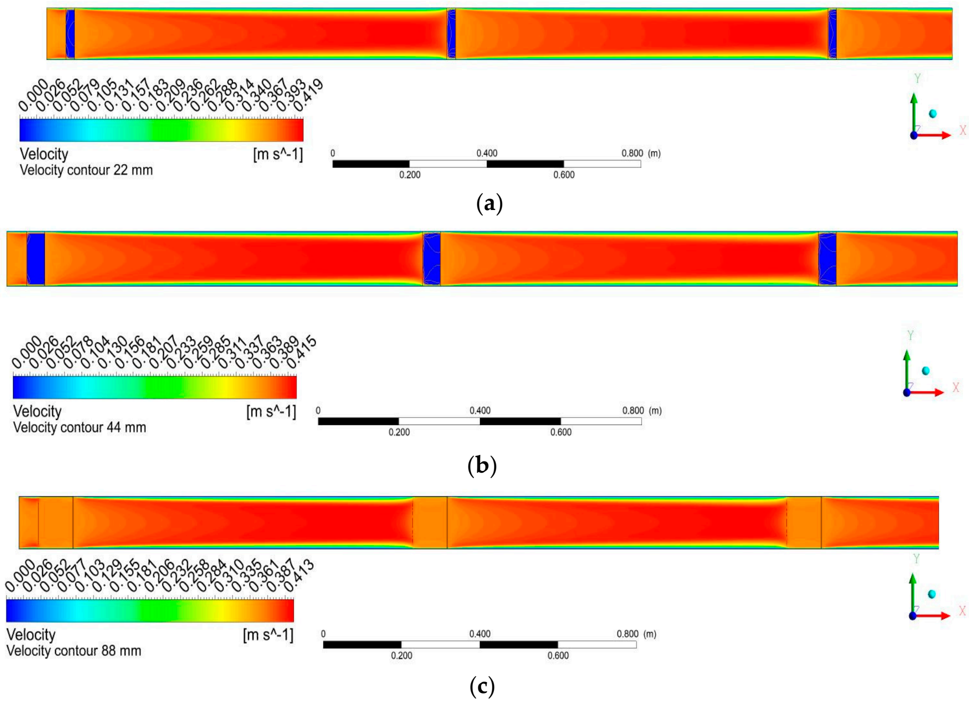

Figure 8. Contour of velocity distribution for 30 PPI 0.92 porosity copper metal foam at 0.3779 m/s velocity for (**a**) 22 mm, (**b**) 44 mm and (**c**) 88 mm thick metal foam.

5.6. Effect of Outlet Temperature and Absorber Plate Temperature

Figure 9a,b shows the variation of temperature with varying mass flow rate from 0.03 to 0.05 kg/s. With 10 PPI with porosity of 0.8769, 20 PPI with a porosity of 0.8567, and 30 PPI with porosity of 0.92 for 22 mm, 44 mm, and 88 mm metal foam thicknesses are considered. It shows that as the mass flow rate and thickness of the metal foam increases, the difference between the absorber plate temperature and bulk fluid temperature reduces. A similar trend is observed for the difference in the absorber plate and outlet temperatures with an increase in mass flow rate. Due to turbulent flow and velocity of air, the difference in the absorber plate and bulk fluid temperature changes. The lower velocity takes more time to travel in the channel, so that the temperature difference increases. Figure 9a shows that the 22 mm 10 PPI copper metal foam has an 8.79% and 11.45% higher average temperature difference of absorber plate temperature and bulk fluid temperature compared to the metal foam of 20 and 30 PPI, respectively. The 44 mm 10 PPI copper metal foam has the same percentage of increase in an average temperature difference of absorber plate temperature and bulk fluid temperature, which is about 3.30% and 3.04% increase for 20 PPI and 30 PPI, respectively. The same trend is observed in 88 mm thickness for 10 PPI compared to 20 PPI and 30 PPI, which is 2.03% and 2.46% higher than 20 PPI and 30 PPI, respectively.

Figure 9b shows that the average temperature difference for 22 mm thickness 10 PPI is higher than all other PPI and all other thicknesses. As the thickness of metal foam increases, the temperature difference between the absorber plate and outlet temperature decreases. As the mass flow rate increase, the temperature difference also decreases. The 22 mm thickness metal foam is having 10.86% and 14.32% more average temperature difference than 20 PPI and 30 PPI, respectively, for the same thickness. The 44 mm, 10 PPI copper metal foam has 4.22% and 3.90% increase in average temperature difference than 20 PPI and 30 PPI, respectively, for the same thickness. The average temperature difference between absorber temperature and outlet temperature of 10 PPI is 2.26% and 3.26% higher than the 20 PPI and 30 PPI of 88 mm metal foam thicknesses.

The above discussion concludes that 10 PPI has a higher temperature difference than 20.

PPI and 30 PPI because of more interfacial surface area of the metal foam. As the thickness of metal foam increases, more conduction occurs near the absorber plate, and hence more heat is transferred to metal foam. So, it is noticed that the average temperature reduces as the thickness of metal foam increases. The empty channel has high average absorber plate temperature than the porous media channel.

5.7. Effect of Heat Transfer Coefficient

Figure 10 shows the heat transfer coefficient variation with respect to different mass flow rate for 10 PPI of 0.8769 porosity, 20 PPI of 0.8567 porosity, and 30 PPI of 0.92 porosity with 22 mm, 44 mm, and 88 mm thicknesses of the metal foam. It is observed that the heat transfer coefficient increases as the mass flow rate increases. As the thickness of the metal foam increases, the heat transfer coefficient also increases. The heat transfer coefficient for 20 PPI 0.8567 porosity and 30 PPI 0.92 porosity is almost in the same range as compared to 10 PPI 0.8769 porosity. The heat transfer coefficient for 10 PPI 0.8769 porosity is less than 20 PPI 0.8567 porosity and 30 PPI 0.92 porosity for all the thicknesses of 22 mm, 44 mm, and 88 mm. The 30 PPI 0.92 porosity has a higher heat transfer coefficient than 10 PPI 0.8769 porosity which is 11.70% for 22 mm thickness, 2.86% for 44 mm thickness, and 2.32% for 88 mm thickness. It is also observed that placing the discrete metal foam and with an increase in thickness of the metal foam the heat dissipation in SAH increases.

5.8. Effect of Nusselt Number

Figure 11 shows that the Nusselt number is directly proportional to the mass flow rate. As the mass flow rate increases, the Nusselt number also increases. With an increase in thickness, the Nusselt number also increases. Figure 11 observes that the 20 PPI of 0.8567 and 30 PPI of 0.92 porosity has a higher Nusselt number compared to 10 PPI of

0.8769 porosity metal foam for 22 mm, 44 mm, and 88 mm thickness of the metal foam. The Nusselt number for 30 PPI of 0.92 porosity is 11.70%, 2.86%, and 2.32% more compared to 10 PPI of 0.8769 porosity for 22 mm, 44 mm, and 88 mm, respectively. The Nusselt number for 20 PPI 0.8567 porosity and 30 PPI 0.92 porosity is almost in the same range for 22 mm, 44 mm, and 88 mm thickness of the metal foam. The results show that with an increase in porosity, the Nusselt number increases because more fluid is flowing through the metal foams.

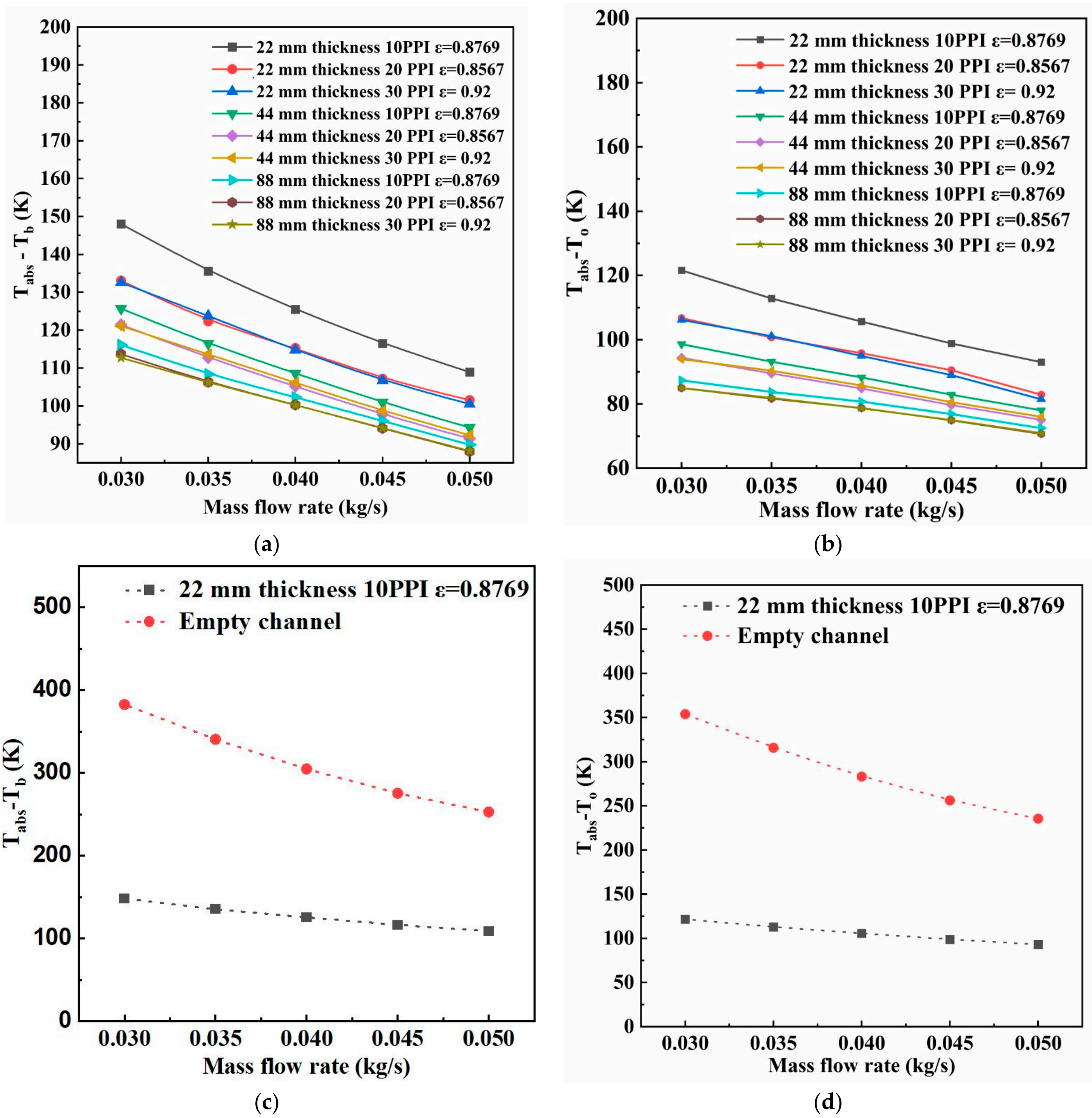

Figure 9. (**a**) Variation of temperature between absorber plate and bulk mean fluid temperature vs. mass flow rate. (**b**) Variation of temperature between absorber plate and outlet temperature vs. mass flow rate. (**c**) Variation of a temperature difference between absorber plate and bulk fluid temperature for empty channel and 22 mm thickness 10 PPI 0.8769 porosity. (**d**) Variation of the temperature difference between absorber plate and outlet temperature for empty channel and 22 mm thickness 10 PPI 0.8769 porosity.

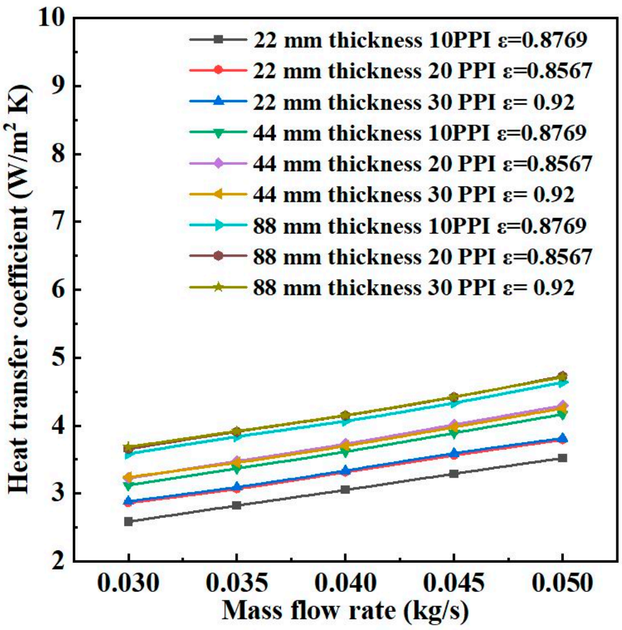

Figure 10. Variation of heat transfer coefficient for different mass flow rates for different PPI and different thickness.

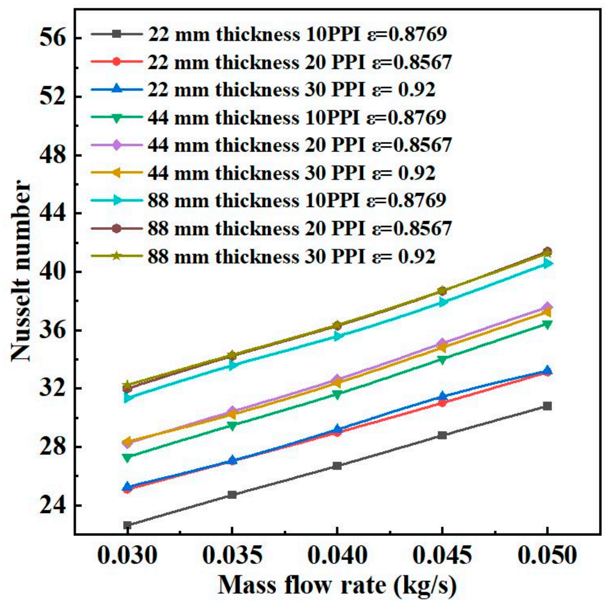

Figure 11. Variation of Nusselt number for different mass flow rates for different PPI and different thicknesses.

5.9. Effect of Pressure Drop

Figure 12 represents that the average pressure drops increase with an increase in the mass flow rate and the thickness of the metal foam 10 PPI, 20 PPI, and 30 PPI of copper metal foam. The average pressure drop is the same for 10 PPI 0.8769porosity and 30 PPI of 0.92 porosity for 22 mm, 44 mm, and 88 mm thick metal foam. The 30 PPI of 0.92 porosity has 28% and 2% more average pressure drop than 20 PPI 0.8567 porosity and 10 PPI 0.8769 porosity, respectively, for 22 mm, 44 mm, and 88 mm thickness. Hence it is concluded that with increase in heat transfer rate, the pressure drop also increases.

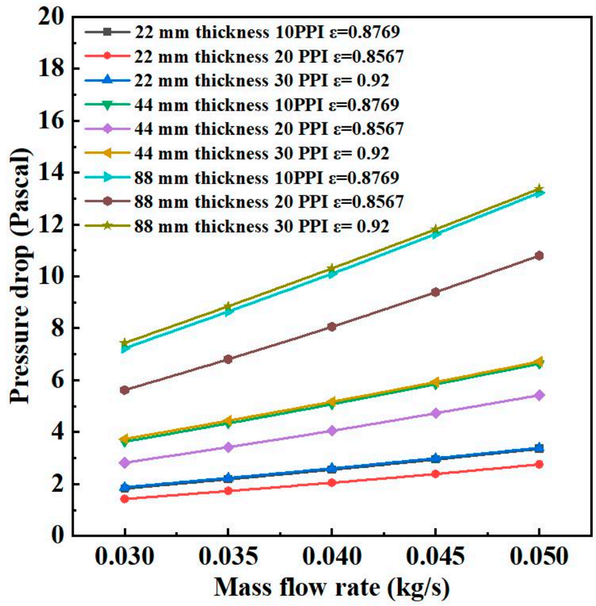

Figure 12. Variation of pressure drop for different mass flow rates for different PPI and different thicknesses.

5.10. Effect of Friction Factor

Figure 13 shows that the friction factor decreases with an increase in mass flow rate. As the thickness of metal foam increases, the friction factor also increases. The 30 PPI 0.92 porosity metal foam has 31% and 2.62% higher friction factor than 20 PPI 0.8567 porosity and 10 PPI 0.8769 porosity copper metal foam for 22 mm, 44 mm, and 88 mm thickness of the metal foam. As the thickness of metal foam increases with twice the value of the previous thickness, the friction factor increases with the same percentage. Hence, it shows that more the PPI, the higher the disturbance to flow, which gives a higher friction factor. The more the thickness of the metal foam, the greater the disturbance of the fluid flow, hence an increase in friction factor.

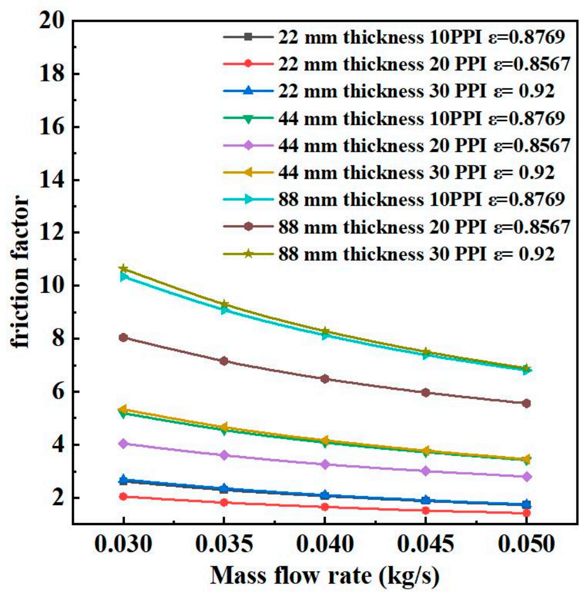

Figure 13. Variation of friction factor for different mass flow rates varying PPI and thickness of metal foam.

5.11. Effect of Ratio of Porous Nusselt Number to Empty Channel Nusselt Number

The heat transfer enhancement ratio is shown in Figure 14. As the PPI and thickness of the metal foam increases, the heat transfer enhancement ratio also increases. The figure represents that with an increase in mass flow rate, the heat transfer enhancement ratio reduces for all cases of PPI and thicknesses. The heat transfer enhancement ratio is higher for lesser velocity than higher velocity because more time is taken for the fluid to flow through the metal foam in lower mass flow rate compared to higher mass flow rate. For 22 mm, 44 mm, and 88 mm, discrete metal foam arrangement in channel shows 30 PPI 0.92 porosity has 11.56%, 3.01%, and 2.41%, respectively, higher than 10 PPI 0.8769 porosity metal foam. With the same 30 PPI 0.92 porosity for an increase in thickness of the metal foam, the heat transfer enhancement increases for 88 mm and 44 mm metal foam thickness which is 12.67% and 10.49%, respectively, more compared to the 22 mm metal foam thickness.

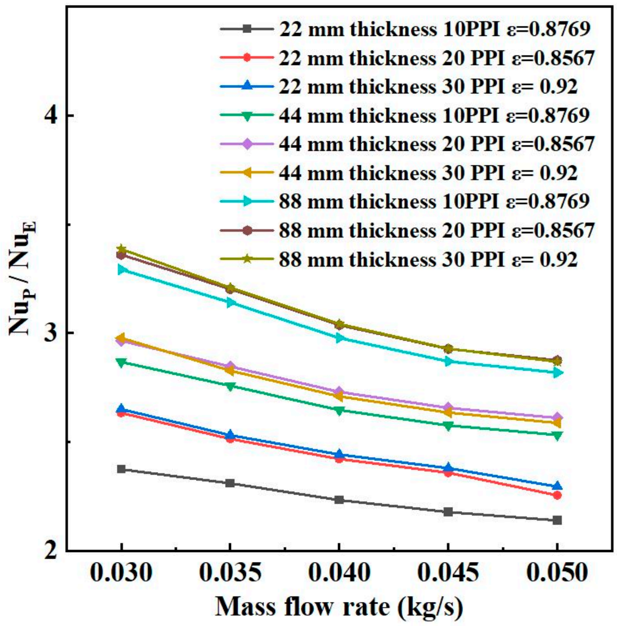

Figure 14. The change in the ratio of Nu_P/Nu_E for different mass flow rates for different PPI and different thicknesses.

5.12. Effect of Performance Factor

Figure 15 shows the performance factor distribution with an increase in mass flow rate. The figure shows that the 22 mm thickness of 20 PPI 0.8567 porosity metal foam is higher than other 44 mm and 88 mm metal foam thickness for 10 PPI 0.8769 porosity and 30 PPI 0.92 porosity. The maximum performance factor for the 20 PPI 0.8567 porosity is 0.0055, 0.0050, and 0.0044 at 22 mm, 44 mm, and 88 mm metal foam thickness, respectively. It is noticed that the performance factor has the maximum value near to 0.0055 at a lower mass flow rate and reduces as the mass flow rate increases.

5.13. Effect of Different Material Metal Foam

Figure 16 shows the difference between different material performance factors. The material considered for comparison is copper, aluminum, and nickel. The figure shows the performance factor for nickel is minimal compared to aluminum and copper. Since copper has high thermal conductivity, the absorber plate and outlet temperature difference are less than nickel. It is observed that the temperature difference reduces as the thermal conductivity increases. The copper metal foam has 3.13% and 9.63% lesser mean temperature difference of the absorber plate temperature and bulk mean fluid temperature than aluminum and nickel, respectively, for 88 mm thick metal foam.

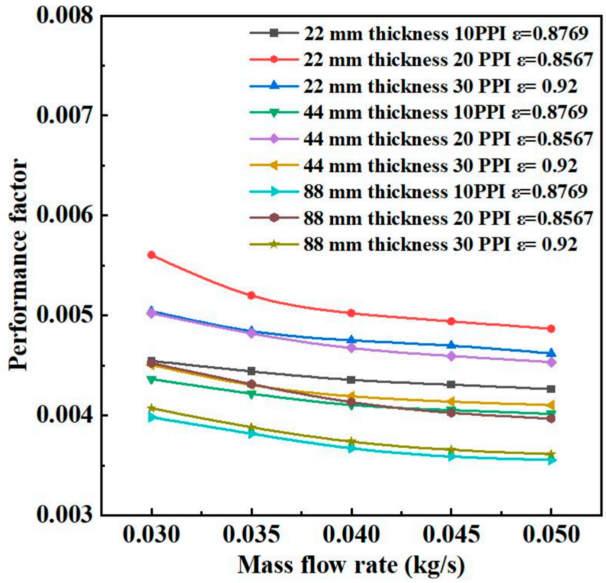

Figure 15. The variation of performance factors for different mass flow rates for different PPI and different thicknesses.

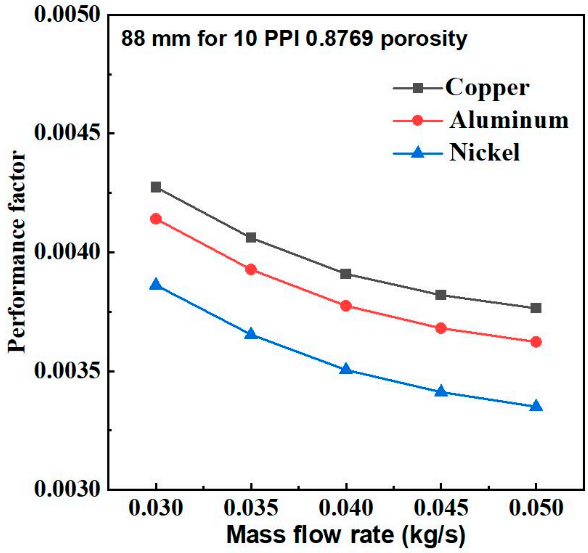

Figure 16. Variation of performance factors for different mass flow rates for different material.

6. Conclusions

The two-dimensional rectangular channel was modelled to evaluate the effect of partial filling of different porosity of copper metal foam in SAH. The complete length of the rectangular channel was 2.35 m and the height was 0.120 m. The computational analysis was performed for three different thicknesses with variation in PPI and porosity of the copper metal foam. Based on the current investigation, the following points are observed:

- With increasing mass flow rate, the outlet temperature decreases for the empty channel as well as for the partially filled porous channel in all cases of PPI and porosity. The same is achieved for different thickness of metal foam. The average temperature difference between the absorber plate and bulk mean fluid temperature is lowest for 88 mm thick metal foam than 22 mm and 44 mm thick metal foam.
- The Nusselt number is higher at higher mass flow rate and rises with increasing PPI and thickness of metal foam. The Nusselt number is highest for 88 mm metal foam, rather than 22 mm and 44 mm thick metal foam The Nusselt number for 22 mm,

44 mm, and 88 mm thicknesses is 157.64%, 183.31%, and 218.60%, respectively, higher than the empty channel.
- The pressure drop increases with higher thickness and it increases with increase in mass flow rate. Amongst the 10 PPI, 20 PPI and 30 PPI copper metal foam, the 20 PPI gives a lesser pressure drop than 10 PPI and 30 PPI metal foam for 22 mm, 44 mm and 88 mm thickness. The highest pressure drop belongs to 30 PPI, having 28% and 2% more average pressure drop than 20 PPI and 10 PPI, respectively, for 22 mm, 44 mm, and 88 mm thickness.
- The performance factor is higher for lower velocity, irrespective of PPI and porosity. The 20 PPI 0.8567 porosity with 22 mm thick metal foam has highest performance factor compared to all 10 PPI and 30 PPI metal foam. For mass flow rate of 0.03 kg/s, the maximum performance factor for the 20 PPI 0.8567 porosity is 0.0055, 0.0050, and 0.0044 at 22 mm, 44 mm, and 88 mm metal foam thickness, respectively.
- The temperature difference of the absorber plate and the bulk mean fluid temperature depend on thermal conductivity of material. The copper has lowest temperature difference of the absorber plate and bulk mean fluid temperature compared to aluminum and nickel because of its thermal conductivity.
- With respect to performance factor, 22 mm 20 PPI 0.8567 porosity is best in terms of pressure drop and cost involved in manufacturing the solar air heater.

The effect of porous media in the heat and fluid flow equations can be included by accounting for permeability, inertia coefficient, and effective thermal conductivity for solid and fluid, effective viscosity and interfacial heat transfer coefficient as well as thermal dispersion. All these parameters depend on porosity, strut diameter and topology of the metal foam. The equations used in this study for determination of permeability, inertia coefficient and interfacial heat transfer coefficient as well as those for effective thermal conductivity for the solid and fluid are calculated based on the porosity and strut diameter for metal foams [11,40]. However, the topology effect should be included for more accurate results by performing a representative elementary analysis.

The current study could be improved by using different geometrical parameters and thermal properties of metal foam. Further, the optimum distance between two discrete metal foams relative to other partially filled scenarios could also be explored.

Author Contributions: Conceptualization, R.D. and N.G.; methodology, R.D., N.G. and M.M.; software, R.D. and N.G.; validation, R.D. and N.G.; formal analysis, R.D. and N.G.; investigation, R.D., N.G. and M.M.; resources, R.D. and N.G.; data curation, R.D.; writing—original draft preparation, R.D.; writing—review and editing, R.D., N.G. and M.M.; visualization, R.D.; supervision, N.G. All authors have read and agreed to the published version of the manuscript.

Funding: This research received no external funding.

Data Availability Statement: Not applicable.

Acknowledgments: The author would like to thank Dnyandeo P. Nathe, Government Polytechnic Nashik Maharashtra 422101 and Abhay Wagh, Technical Education Maharashtra, Higher and Technical Education, Government of Maharashtra for giving the opportunity to do research under the quality improvement programme (QIP) in Mechanical Engineering Department, National Institute of Technology Surathkal Karnataka India. The author is also thankful to AICTE India for providing the QIP scheme facility.

Conflicts of Interest: The authors declare no conflict of interest between the contents of this work and any reported studies.

Nomenclature

A_C	Collector area in (m^2)
A_p	Absorber plate area in (m^2)
a, b	Constants for monthly average daily global radiation
a_{sf}	Interfacial surface area (m^{-1})
CFD	Computational fluid dynamics
CI	Inertial form coefficient
Cp	Specific heat of fluid (J/kg K)
Ct	Constant for top loss coefficient
d	The spacing between the glass cover and absorber plate (m)
D_h	Hydraulic diameter
d_f	Fibre diameter (m)
d_p	Pore diameter (m)
ΔP	The pressure drops across the collector in Pa.
FPSC	Flat plate Solar collector
$\acute{F}$	The solar air heater efficiency factor
F_R	The solar air heater heat removal factor
f	Friction factor
f_c	Normalizing factor
f_t	Constant for top loss coefficient
HTC	Heat transfer coefficient (W/m^2 K)
$\overline{H_d}$	Monthly average of the daily diffuse radiation on a horizontal surface (kJ/m^2-day)
$\overline{H_g}$	Monthly average of the daily global radiation on a horizontal surface at a location (kJ/m^2-day)
H_0	The daily radiation falls on a horizontal surface at the location, kJ/m^2
$\overline{H_o}$	The mean value of global radiation for each day of the month, kJ/m^2
h	Heat transfer coefficient (W/m^2 K)
$\overline{h}$	Average heat transfer coefficient, W/m^2 K
h_e	The effective heat transfer coefficient W/m^2 K
hfp	The convective heat transfer coefficient between the absorber plate and the air stream, W/m^2 K
h_r	The radiative heat transfer coefficient (W/m^2 K)
h_{sf}	Interfacial heat transfer coefficient
h_w	The convective heat transfer coefficient at the top cover, W/m^2 K
I_b	Beam radiation, W/m^2
I_d	Diffuse radiation, W/m^2
$\overline{I_d}$	Monthly average of the hourly diffuse radiation on a horizontal surface (kJ/m^2-h)
$\overline{I_g}$	Monthly average of the hourly global radiation on a horizontal surface (kJ/m^2-h)
I_g	Global radiation, W/m^2
$\overline{I_o}$	Monthly average of the hourly extraterrestrial radiation on a horizontal surface (kJ/m^2-h)
I_{SC}	Spectral distribution of extraterrestrial solar radiation flux at mean sun-earth distance (W/m^2)
I_T	The total flux falling on a tilted surface at any instant (W/m^2)
j	Colburn j factor
K	Permeability (m^2)
k_{air}	Thermal conductivity of air (W/m K)
k_i	The thermal conductivity of insulation material (W/m K)
L	Length of the solar air heater (m)
LTE	Local thermal equilibrium
LTNE	Local thermal nonequilibrium model
M	Number of glass covers
$\dot{m}$	Mass flow rate kg/s
Nu	Nusselt number
Nu_P	Nusselt number of porous media
Nu_E	Nusselt number of empty channel
n	The day of the year
PPI	Pores per inch

Pr	Prandtl number
q	Heat flux (W/m^2)
q_u	Useful heat gain (W/m^2)
Re	Reynolds number
Re_{d_f}	Reynolds number by fiber diameter
Re_p	Reynolds number for porous media
RNG	Renormalization Group
r_b	The tilt factor for beam radiation
r_d	The tilt factor for diffuse radiation
r_r	The tilt factor for reflector radiation
SAH	Solar air heater
SWH	Solar water heater
S	The flux absorbed in the absorber plate (W/m^2)
$\overline{S}$	Monthly average of the sunshine hours per day at the location, hr
$\overline{S_{max}}$	The daily sunlight or sunshine hours per day
ω_s	The hour angle at sunrise or sunset on the horizontal surface in degree
ω_{st}	The hour angle at sunrise or sunset
T_{bm}	Mean bottom plate temperature in K
Tfi	The inlet temperature of the fluid in K
T_{fo}	The outlet temperature of a fluid in K
T_{pm}	Mean plate temperature in K
U_b	The bottom loss coefficient of solar air heater (W/m^2 K)
U_L	The overall loss coefficient (W/m^2 K)
U_s	The side loss coefficient (W/m^2 K)
U_t	The top loss coefficient fir solar air heater (W/m^2- K)
u	The velocity of fluid (m/s)
V_∞	Wind velocity m/s
V	The average air velocity in m/s
W	The width of absorber plate in m
η_P	Performance factor
η_i	The instantaneous efficiency of the solar air heater
δ	Declination, in degree i.e., the angle made by the line joining the centers of the sun and the earth with the projection of this line on the equatorial plane
δ_b	The thickness of insulation material in m
Greek symbols	
ε	Porosity
ε_C	Glass cover emissivity
ε_P	Absorber plate emissivity
ε_b	Bottom plate emissivity
θ	The angle between an incident solar beam flux and the normal to a plane surface
β	The slope of the solar air heater with the horizontal surface.
Φ	Latitude of a location
λ_f	Thermal conductivity of the fluid W/m K
k	Thermal conductivity (W/m K)
ν	Kinematic viscosity (m^2/s)
ρ	Density of the fluid (kg/m^3)
σ	Stefan Boltzmann constant
τ	The transmissivity of the cover system of solar air heater
τ_a	The transmissivity obtained by considering only absorption
τ_r	The transmissivity obtained by considering only reflection and refraction
μ	Dynamic viscosity (kg/ms)
Subscript	
Abs	Absorber
b	Bulk mean fluid
f	fluid
i	Inlet
max	maximum

o	Outlet
s	Solid

References

1. Kansara, R.; Pathak, M.; Patel, V.K. Performance Assessment of Flat-Plate Solar Collector with Internal Fins and Porous Media through an Integrated Approach of CFD and Experimentation. *Int. J. Therm. Sci.* **2021**, *165*, 106932. [CrossRef]
2. Sukhatme, S.P. *Solar Energy*, 4th ed.; McGraw Hill: New York, NY, USA, 2018.
3. Garg, H.P. *Solar Energy Fundamentals and Applications*, 1st ed.; Mc Graw Hill: New York, NY, USA, 2016.
4. Ismael, M.A. Forced Convection in Partially Compliant Channel with Two Alternated Baffles. *Int. J. Heat Mass Transf.* **2019**, *142*, 118455. [CrossRef]
5. Jadhav, P.H.; Gnanasekaran, N.; Mobedi, M. Analysis of Functionally Graded Metal Foams for the Accomplishment of Heat Transfer Enhancement under Partially Filled Condition in a Heat Exchanger. *Energy* **2023**, *263*, 125691. [CrossRef]
6. Abd Al-Hassan, A.Q.; Ismael, M.A. Numerical Study of Double Diffusive Mixed Convection in Horizontal Channel with Composite Open Porous Cavity. *Spec. Top. Rev. Porous Media Int. J.* **2019**, *10*, 401–419. [CrossRef]
7. Ali Abd Al-Hassan, M.I. Effect of Triangular Porous Layer on the Transfer of Heat and Species in a Channel-open Cavity. In *Heat Transfer*; Wiley: New York, NY, USA, 2022. [CrossRef]
8. García-Moreno, F. Commercial Applications of Metal Foams: Their Properties and Production. *Materials* **2016**, *9*, 85. [CrossRef]
9. Trilok, G.; Gnanasekaran, N.; Mobedi, M. Various Trade-Off Scenarios in Thermo-Hydrodynamic Performance of Metal Foams Due to Variations in Their Thickness and Structural Conditions. *Energies* **2021**, *14*, 8343. [CrossRef]
10. Jadhav, P.H.; Trilok, G.; Gnanasekaran, N.; Mobedi, M. Performance Score Based Multi-Objective Optimization for Thermal Design of Partially Filled High Porosity Metal Foam Pipes under Forced Convection. *Int. J. Heat Mass Transf.* **2022**, *182*, 121911. [CrossRef]
11. Jadhav, P.H.; Gnanasekaran, N.; Perumal, D.A. Numerical Consideration of LTNE and Darcy Extended Forchheimer Models for the Analysis of Forced Convection in a Horizontal Pipe in the Presence of Metal Foam. *J. Heat Transf.* **2021**, *143*, 012702. [CrossRef]
12. Sharma, S.P.; Saini, J.S.; Varma, H.K. Thermal Performance of Packed-Bed Solar Air Heaters. *Sol. Energy* **1991**, *47*, 59–67. [CrossRef]
13. Rajarajeswari, K.; Alok, P.; Sreekumar, A. Simulation and Experimental Investigation of Fluid Flow in Porous and Non-Porous Solar Air Heaters. *Sol. Energy* **2018**, *171*, 258–270. [CrossRef]
14. Singh, S.; Dhruw, L.; Chander, S. Experimental Investigation of a Double Pass Converging Finned Wire Mesh Packed Bed Solar Air Heater. *J. Energy Storage* **2019**, *21*, 713–723. [CrossRef]
15. Kesavan, S.; Arjunan, T.V.; Vijayan, S. Thermodynamic Analysis of a Triple-Pass Solar Dryer for Drying Potato Slices. *J. Therm. Anal. Calorim.* **2019**, *136*, 159–171. [CrossRef]
16. Sözen, A.; Şirin, C.; Khanlari, A.; Tuncer, A.D.; Gürbüz, E.Y. Thermal Performance Enhancement of Tube-Type Alternative Indirect Solar Dryer with Iron Mesh Modification. *Sol. Energy* **2020**, *207*, 1269–1281. [CrossRef]
17. Singh, S. Experimental and Numerical Investigations of a Single and Double Pass Porous Serpentine Wavy Wiremesh Packed Bed Solar Air Heater. *Renew. Energy* **2020**, *145*, 1361–1387. [CrossRef]
18. Srinivas, K.E.S.; Harikrishnan, D.; Mobedi, M. Correlations and Numerical Modeling of Stacked Woven Wire-Mesh Porous Media for Heat Exchange Applications. *Energies* **2022**, *15*, 2371.
19. Li, X.; Yuan, F.; Tian, W.; Dai, C.; Yang, X.; Wang, D.; Du, J.; Yu, W.; Yuan, H. Heat Transfer Enhancement of Nanofluids with Non-Spherical Nanoparticles: A Review. *Appl. Sci.* **2022**, *12*, 4767. [CrossRef]
20. Mortazavifar, S.L.; Salehi, M.R.; Shahraki, M.; Abiri, E. Optimization of Light Absorption in Ultrathin Elliptical Silicon Nanowire Arrays for Solar Cell Applications. *J. Mod. Opt.* **2022**, *69*, 368–380. [CrossRef]
21. Sezer, N.; Khan, S.A.; Biçer, Y.; Koç, M. Enhanced Nucleate Boiling Heat Transfer on Bubble-Induced Assembly of 3D Porous Interconnected Graphene Oxide/Silver Nanowire Hybrid Network. *Case Stud. Therm. Eng.* **2022**, *38*, 102334. [CrossRef]
22. Kamath, P.M.; Balaji, C.; Venkateshan, S.P. Convection Heat Transfer from Aluminium and Copper Foams in a Vertical Channel—An Experimental Study. *Int. J. Therm. Sci.* **2013**, *64*, 1–10. [CrossRef]
23. Bayrak, F.; Oztop, H.F. Experimental Analysis of Thermal Performance of Solar Air Collectors with Aluminum Foam Obstacles Kapali Hücreli Alüminyum Köpük Engeller Sahip Hava Isitmali Güneş Kollektörlerinin Isil Performansinin Deneysel Analizi. *J. Therm. Sci. Technol.* **2015**, *35*, 11–20.
24. Dukhan, N.; Quinones, P.D. Convective Heat Transfer Analysis of Open Cell Metal Foam for Solar Air Heaters. *Int. Sol. Energy Conf.* **2003**, *36762*, 287–293.
25. Mancin, S.; Zilio, C.; Diani, A.; Rossetto, L. Experimental Air Heat Transfer and Pressure Drop through Copper Foams. *Exp. Therm. Fluid Sci.* **2012**, *36*, 224–232. [CrossRef]
26. Chen, C.C.; Huang, P.C. Numerical Study of Heat Transfer Enhancement for a Novel Flat-Plate Solar Water Collector Using Metal-Foam Blocks. *Int. J. Heat Mass Transf.* **2012**, *55*, 6734–6756. [CrossRef]
27. Jouybari, H.J.; Saedodin, S.; Zamzamian, A.; Nimvari, M.E.; Wongwises, S. Effects of Porous Material and Nanoparticles on the Thermal Performance of a Flat Plate Solar Collector: An Experimental Study. *Renew. Energy* **2017**, *114*, 1407–1418. [CrossRef]
28. Saedodin, S.; Zamzamian, S.A.H.; Nimvari, M.E.; Wongwises, S.; Jouybari, H.J. Performance Evaluation of a Flat-Plate Solar Collector Filled with Porous Metal Foam: Experimental and Numerical Analysis. *Energy Convers. Manag.* **2017**, *153*, 278–287. [CrossRef]

29. Hussien, S.Q.; Farhan, A.A.; Hussien, S.Q.; Farhan, A.A. Research The Effect of Metal Foam Fins on the Thermo-Hydraulic Performance of a Solar Air Heater. *Int. J. Renew. Energy* **2019**, *9*, 840–847.
30. Baig, W.; Ali, H.M. An Experimental Investigation of Performance of a Double Pass Solar Air Heater with Foam Aluminum Thermal Storage Medium. *Case Stud. Therm. Eng.* **2019**, *14*, 100440. [CrossRef]
31. Anirudh, K.; Dhinakaran, S. Performance Improvement of a Flat-Plate Solar Collector by Inserting Intermittent Porous Blocks. *Renew. Energy* **2020**, *145*, 428–441. [CrossRef]
32. Farhan, A.A.; Obaid, Z.A.H.; Hussien, S.Q. Analysis of Exergetic Performance for a Solar Air Heater with Metal Foam Fins. *Heat Transf.-Asian Res.* **2020**, *49*, 3190–3204. [CrossRef]
33. Anirudh, K.; Dhinakaran, S. Numerical Analysis of the Performance Improvement of a Flat-Plate Solar Collector Using Conjugated Porous Blocks. *Renew. Energy* **2021**, *172*, 382–391. [CrossRef]
34. Jadhav, P.H.; Nagarajan, G.; Perumal, D.A. Conjugate Heat Transfer Study Comprising the Effect of Thermal Conductivity and Irreversibility in a Pipe Filled with Metallic Foams. *Heat Mass Transf. Und Stoffuebertragung* **2021**, *57*, 911–930. [CrossRef]
35. Yadav, S.; Saini, R.P. Numerical Investigation on the Performance of a Solar Air Heater Using Jet Impingement with Absorber Plate. *Sol. Energy* **2020**, *208*, 236–248. [CrossRef]
36. Chen, Z.; Gu, M.; Peng, D. Heat Transfer Performance Analysis of a Solar Flat-Plate Collector with an Integrated Metal Foam Porous Structure Filled with Paraffin. *Appl. Therm. Eng.* **2010**, *30*, 1967–1973. [CrossRef]
37. Yadav, A.S.; Bhagoria, J.L. Heat Transfer and Fluid Flow Analysis of Solar Air Heater: A Review of CFD Approach. *Renew. Sustain. Energy Rev.* **2013**, *23*, 60–79. [CrossRef]
38. *Ansys Fluent R2 Student Version*; Ansys, Inc.: Canonsburg, PA, USA, 2022.
39. Vafai, K. *Handbook of Porous Media*, 2nd ed.; CRC Press: Boca Raton, FL, USA, 2005.
40. Calmidi, V.V.; Mahajan, R.L. Forced Convection in High Porosity Metal Foams. *J. Heat Transf.* **2000**, *122*, 557–565. [CrossRef]
41. Sharma, S.; Talukdar, P. Thermo-Mechanical Analysis of a Porous Volumetric Solar Receiver Subjected to Concentrated Solar Radiation. *Sol. Energy* **2022**, *247*, 41–54. [CrossRef]
42. Zhang, S.; Yao, Y.; Jin, Y.; Shang, Z.; Yan, Y. Heat Transfer Characteristics of Ceramic Foam/Molten Salt Composite Phase Change Material (CPCM) for Medium-Temperature Thermal Energy Storage. *Int. J. Heat Mass Transf.* **2022**, *196*, 123262. [CrossRef]
43. Cengel, Y.A. *Heat Transfer a Practical Approach*; McGraw-Hill: New York, NY, USA, 2003.